Intraseasonal variability of the South Vietnam Upwelling, South China Sea: influence of atmospheric forcing and ocean intrinsic variability.

Marine Herrmann[1*], Thai To Duy[2], Claude Estournel[1]

[1] Université de Toulouse, LEGOS (IRD/CNES/CNRS/UPS), Toulouse, France, 31400 Toulouse, France

[2] Institute of Oceanography (IO), Vietnam Academy of Science and Technology (VAST), Nha Trang, Vietnam

Correspondence to : Marine Herrmann (marine.herrmann@ird.fr)

Short summary

The South Vietnam Upwelling develops in summer along and off the Vietnamese coast. It brings cold and nutrient-rich waters to the surface, allowing photosynthesis essential to marine ecosystems and fishing resources. We show here that its daily variations are mainly due to the wind, thus predictable, in the southern shelf and coast regions. However, they are more chaotic in the offshore area, and especially in the northern area, due to the influence of eddies of a highly chaotic nature.

15   **Abstract**

16   The South Vietnam Upwelling (SVU) develops off the Vietnamese coast (South China Sea) during the southwest

17   summer monsoon over four main areas: the northern coastal upwelling (NCU), the southern coastal upwelling

18   (SCU), the offshore upwelling (OFU) and the shelf off the Mekong River mouth (MKU). An ensemble of ten

19   simulations with perturbed initial conditions were run with the fine-resolution SYMPHONIE model (1 km

20   inshore) to investigate the daily to intraseasonal variability of the SVU and the influence of the ocean intrinsic

21   variability (OIV) during the strong SVU of summer 2018.

22   The intraseasonal variability is similar for SCU, MKU and OFU, driven to the first order by the wind variability.

23   MKU and SCU are induced by stable ocean dynamics (the northeastward then eastward boundary current) and

24   have very little chaotic variability. The OIV has a stronger influence on OFU. In July, OFU mainly develops along

25   the northern flank of the eastward jet. The influence of OIV is strongest and related to the chaotic variability of

26   the meridional position of the jet. In August this position is stable and OFU develops mainly in the area of positive

27   wind curl and cyclonic eddies north of the jet. The influence of OIV, weaker than in July, is related to the

28   organization of this mesoscale circulation. NCU shows a behavior different from that observed in the other areas.

29   In the heart of summer, a large-scale circulation formed by the eastward jet and eddy dipole is well established

30   with an alongshore current preventing NCU development. In early and late summer, this circulation is weaker,

31   allowing a mesoscale circulation of strongly chaotic nature to develop in the NCU area. During those periods, the

32   OIV influence on NCU is very strong and related to the organization of this mesoscale circulation: NCU is favored

33   (annihilated) by offshore-oriented (alongshore) structures.

34

1.   Introduction

36   The summer general circulation in the central South China sea is largely induced by the prevailing southwest

37   monsoon winds (Wang et al., 2004; Wyrtki et al., 1961). It is characterized by the development off the central

38   Vietnamese coast of an anticyclonic (AC) gyre in the south and a cyclonic (C) gyre in the north (forming an eddy

39   dipole referred to as the ACC dipole) and of the South Vietnam upwelling, hereafter referred to as the SVU, that

40   develops over four main areas. First, the convergence of two gyres creates an eastward jet departing from the

41   southern part of the central coast of Vietnam between 11°N and 12°N. This convergence gives rise to an Ekman

42   current-induced coastal upwelling (Dippner et al., 2007; Chen et al., 2012), hereafter referred to as SCU. Second,

43   Ekman pumping-induced upwelling (OFU hereafter) develops offshore in the area of strong positive wind and

44   surface current vorticity (Liu et al., 2012; Da et al., 2019; Ngo and Hsin, 2021). Third, recent studies have revealed

45   that coastal upwelling (NCU hereafter) can develop along the northern part of the central Vietnamese coast (Da

46   et al., 2019; Ngo and Hsin, 2021; To Duy et al., 2022). Last, To Duy et al. (2022) showed for the first time that

47   upwelling develops off the Mekong Delta behind Con Dao islands (see Fig. 1b, MKU hereafter). SVU participates

48   in the nutrient enrichment of the surface layer, hence plays an important role in the biological productivity and in

49   the halieutic resources of the region (Bombar et al., 2010; Liu et al., 2012; Loick-Wilde et al., 2017; Lu et al.,

50   2018; Loisel et al., 2017). Some authors also showed that the SVU may influence the functioning of local and

51   regional climate (Xie et al., 2003; Zheng et al., 2016). Understanding precisely the functioning and variability of

52   the SVU and its response to long-term changes is therefore an important issue.

The interannual variability of the SVU has been investigated in numerous previous studies. In the SCU, OFU and MKU regions, the interannual variability of summer wind intensity is related to and in phase with the intensity of the summer monsoon, and is the main driver of the interannual variability of upwelling intensity (Wang et al., 2006; Chen et al., 2014; Li et al., 2014; Da et al., 2019; Ngo and Hsin, 2021; To Duy et al., 2022). ENSO (El Niño Southern Oscillation) also impacts the upwelling in those regions, due to its influence on summer monsoon wind (Wang et al., 2006; Kuo et al., 2004; Loick-Wilde et al., 2017; Da et al., 2019). Some studies (Li et al., 2014; Da et al., 2019) then revealed that ocean intrinsic variability (OIV) influences the interannual variability of the eastward jet and of the OFU. OIV, as opposed to the forced variability, corresponds to the unpredictable part of ocean variability, not induced by the variability of external forcing factors but by the chaotic behavior of ocean dynamics. Most studies have shown that mesoscale to submesoscale structures are a major source of OIV (Penduff et al., 201; Sérazin et al., 2016; Waldman et al., 2018; Da et al. 2019). This influence of OIV is related to the spatial distribution of summer averaged surface current vorticity associated with eddies: cyclonic (anticyclonic) eddies located in the area of positive wind stress curl enhance (weaken) the Ekman pumping-induced OFU. The interannual variability of NCU shows a completely different behavior. Ngo and Hsin (2021) and To Duy et al. (2022) concluded that wind conditions favorable to SCU, MKU and OFU were unfavorable to NCU, and vice versa. To Duy et al. (2022) moreover showed that the influence of wind is weaker for NCU than for the other areas. In contrast, the influence of circulation, in particular of the spatial organization of the chaotic submesoscale to mesoscale circulation that prevails over the area, was found to be stronger: on a seasonal average, NCU is inhibited when alongshore currents prevail, and enhanced when offshore circulation prevails.

The daily to intraseasonal variability of the SVU was much less studied. Available studies, all based on satellite data, focused on the SCU and OFU. Xie et al. (2007) showed that the upwelling in those areas does not develop smoothly during the summer, but shows a strong intraseasonal variability related to the wind variability and Madden Julian Oscillation (MJO). They suggested that SVU experiences two to four events of development and decay during the summer, in response to the wind fluctuations. Isoguchi and Kawamura (2006) and Liu et al. (2012) confirmed respectively for the period 2000-2002 and for summer 2007 that the MJO is a strong driver of the events of southwesterly wind intensification within the season and of the resulting upwelling. They moreover revealed the effect of tropical storms that can reinforce the southwesterly wind, hence the SVU.

To better understand the functioning and variability of the SVU, it is therefore necessary to investigate in detail the functioning of its daily to intraseasonal variability over its four areas of development (SCU, NCU, OFU and MKU) and to identify the driving factors. Previous studies mentioned above revealed the role of wind for SCU and OFU, which should be examined for the other areas. The role of OIV in the interannual variability of the upwelling, related to mesoscale circulation and eddies in the coastal and offshore area, was highlighted for OFU and suggested for NCU. It should be examined at the intraseasonal scale, and requires an ensemblist approach as used by Waldman et al. (2017a, 2018). Chen et al. (2012) also showed from idealized simulations that tides and river plumes could be also involved in SVU variability; however, to our knowledge, only very few models used for the SVU study included the effect of tides, and none of them investigated their impact.

The present paper focuses on the daily to intraseasonal variability of the SVU over its four areas of development, examining in particular the role of atmospheric forcing, in particular wind, and the role of ocean dynamics and their intrinsic variability. The effect of tides and rivers will be examined in a future study. A fine-resolution

92   realistic model including tides and already presented and evaluated in To Duy et al. (2022) for the period 2009-

93   2018 is used. Ensemble simulations with perturbed initial conditions are performed to study the case of summer

94   2018, which was an exceptionally strong summer of upwelling for SCU, OFU and MKU (Ngo and Hsin, 2021;

95   To Duy et al., 2022).

96   The fine-resolution model and ensemble simulations and the definition of study areas, upwelling indicators and

97   OIV indicators are presented in Section 2. The intraseasonal variability of the oceanic circulation and of the SVU,

98   including the role of OIV, are examined respectively in Section 3 and Section 4. Results are summarized and

99   future work is discussed in Section 5.

100

2. Methodology

2.1. The 3-D hydrodynamical ocean model SYMPHONIE

103   To Duy et al. (2022) built a fine-resolution configuration of the 3-D ocean circulation model SYMPHONIE

104   (Marsaleix et al., 2008, 2019) over the Vietnam coastal region (VNC hereafter for VietNam Coast), based on a

105   horizontal polar grid with a resolution decreasing linearly seaward, from 1 km at the Vietnamese coast to 4.5 km

106   offshore, and with 50 vertical levels. They used the GEBCO_2014 dataset released in April 2015 at a 30 seconds

107   interval (~0.9 km) and available from www.gebco.net. We use exactly the same configuration here and show

108   VNC domain in Figure 1a,b. The atmospheric forcing is computed from the 3-hourly output of the European

109   Center for Medium-Range Weather Forecasts (ECMWF) 1/8° atmospheric analysis, distributed on

110   http://www.ecmwf.int. Initial and lateral ocean boundary conditions are prescribed from the daily outputs of the

111   global ocean 1/12° analysis PSY4QV3R1 distributed by the Copernicus Marine and Environment Monitoring

112   Service (CMEMS) on http://marine.copernicus.eu. The implementation of tides follows Pairaud et al. (2008, 2010)

113   and considers the 9 main tidal harmonics, provided by the 2014 release of the FES global tidal model (Lyard et

114   al., 2006). Freshwater discharge is provided for 36 river mouths. More details about the model, its configuration

115   and the forcings are provided in To Duy et al. (2022). They performed and evaluated a 10-year simulation over

116   the period 2009-2018, hereafter called LONG, showing that it reproduces realistically the temporal (seasonal to

117   interannual) and spatial variability of the SCS ocean dynamics and water masses. In the LONG simulation, a very

118   strong SVU developed during summer 2018, in particular due to strong July-August northeastward wind (To Duy

119   et al., 2022).

2.2. Ensemble simulations

121   We performed an ensemble of ten simulations with perturbed initial conditions between January 1st, 2017 and

122   December 31st, 2018. For that we used ten different initial conditions for temperature, salinity, sea surface

123   elevation and currents fields. Most of the OIV develops at mesoscale (Sérazin et al., 2015, Waldman et al., 2018),

124   we therefore only perturbed the mesoscale field, following the same methodology as Waldman et al. (2017a,

125   2017b, 2018). For the ten simulations of the ensemble, the large-scale state of the initial field is identical, and the

126   small-scale of the initial field state differs. The common large-scale state is equal to the large-scale state of January

127   1st, 2017 of the LONG simulation, computed using a 100 km low-pass filter. For XX going from 09 to 18, the

128   small-scale state of January 1st, 20XX of the LONG simulation is computed using a 100 km high-pass filter. The

129 initial state of member XX of the simulation ensemble is then computed by adding this small-scale state to the
130 common large-scale state.

2.3. Definition of upwelling areas

132 Figure 1c,d shows the SST averaged over June-September (JJAS) 2018 for the ensemble average and for OSTIA
133 (Operational Sea Surface Temperature and Sea Ice Analysis) reanalysis outputs, available at
134 ftp://data.nodc.noaa.gov/pub/data.nodc/ghrsst/L4/GLOB/UKMO/OSTIA/. Simulated SST is in good agreement
135 with observations, showing a large area of colder surface water corresponding to the strong SVU that developed
136 during summer 2018. We show in Figure 1b,c,d the four boxes used by To Duy et al. (2022), that correspond to
137 the four main areas of SVU development: boxSC and boxNC for respectively the southern (SCU) and northern
138 (NCU) coastal upwelling, boxOF for the offshore upwelling (OFU), and boxMK for the upwelling offshore the
139 Mekong delta (MKU).

2.4. Indicators of upwelling intensity

141 We compute a SST-based index of upwelling intensity following exactly the same methodology as Da et al. (2019)
142 and To Duy et al. (2022). The daily upwelling index UI_d is computed every day t at each point (x,y) of the study
143 area that verifies $SST(x,y,t)<T_o$ as:

144 $$UI_d(x,y,t) = T_{ref} - SST(x,y,t) \text{ for (x,y,t) where SST(x,y,t)} < T_o \tag{1}$$

145 The reference temperature T_{ref}= 29.2°C is computed as the SST averaged over JJAS and over boxT$_{Ref}$, the area
146 east of the upwelling region that is the least impacted by upwelling (see Figure 1c,d), in the LONG simulation.
147 The threshold temperature under which upwelling occurs, T_0= 27.6°C, is defined as the optimal upwelling
148 threshold that covers the largest number of upwelling occurrences but avoids to include cold water horizontally
149 advected between upwelling areas.

150 For each box $boxN$, the daily intensity of upwelling integrated over $boxN$ is quantified at day t by the daily
151 upwelling index $UI_{d,boxN}$, computed as:

152 $$UI_{d,boxN}(t) = \frac{\iint_{(x,y) \text{ in boxN so that } SST(x,y,t)<T_0}(T_{ref}-SST(x,y,t)).dx.dy}{A_{boxN}} \tag{2}$$

153 where A_{boxN} is the size of $boxN$.

154 Last, to quantify the intensity of upwelling integrated over boxN and over the summer, we define the summer
155 upwelling index $UI_{JJAS,boxN}$, computed over JJAS as:

156 $$UI_{JJAS,boxN} = \frac{\int_{JJAS} UI_{d,boxN}(t)dt}{ND_{JJAS}} \tag{3}$$

157 where ND_{JJAS} = 122 days is the JJAS duration.

2.5. Indicators of OIV impact

Following Waldman et al. (2018), we introduce two indicators to quantify the contribution of OIV on a given variable X : one at the daily scale and one at the average scale over a given period. $X(t,i)$ at time t and for ensemble member i can be any time-dependent (space-dependent or not) variable characterizing the ocean circulation or upwelling intensity. In the following, σ_i is the ensemble standard deviation (that quantifies the time-dependent intrinsic variability), σ_t temporal standard deviation, m_i the ensemble average and m_t the temporal average.

We quantify the effect of OIV at the daily scale by computing IV_d, the contribution of intrinsic variability to the total daily variability of $X(t,i)$. For each day of JJAS 2018, it is computed as the ratio between the time-dependent intrinsic variability and the total temporal variability over JJAS 2018:

$$IV_d\big(X(t)\big) = \frac{\sigma_i\big(X(t,i)\big)}{\sqrt{m_i\big(\sigma_t\big(X(t,i)\big)^2\big)}} \tag{6}$$

We quantify the contribution of OIV at the average scale over a given period by computing the relative intrinsic variability of the temporal mean state of X over the period, IV_{tm}. For that, we compute the ratio between the ensemble standard deviation and the ensemble average of temporal average of $X(t,i)$:

$$IV_{tm}(X) = \frac{\sigma_i\big(m_t\big(X(t,i)\big)\big)}{m_i\big(m_t\big(X(t,i)\big)\big)} \tag{5}$$

To investigate the effect of OIV on surface circulation and upwelling, we apply in the following those indicators on the upwelling indices (UI_d, $UI_{d,boxN}$ and $UI_{JJAS,boxN}$) and on the surface current vorticity.

3. Intraseasonal variability of wind and ocean circulation

Figure 2 shows for each upwelling area the daily time series of wind stress, of $UI_{d,boxN}$ for each simulation and for the ensemble average, and of $IV_d(UI_{d,boxN})$. The southwest summer monsoon wind blows from June to September over the SCS with three main peaks of strong northeastward wind during mid-June, beginning to mid-July and beginning of August, associated with three peaks of OFU, SCU and MKU that will be examined in detail in Section 4 (see the daily time series of $UI_{d,boxN}$ and wind stress averaged over boxOF, boxSC and boxMK, Figure 2a,b,c). To study the development of upwelling and the ocean circulation over those areas, we define three periods that fully cover OFU development (from a value of UId,boxOF=0 to a maximum value) : June (9th-18th June, 10 days), July (28th June-18th July, 21 days) and August (1st-13th August, 13 days), highlighted in blue in Figure 2. The development of OFU, SCU and MKU follows a similar chronology and the exact choice of each periods did not modify our conclusions, as long as those periods cover the upwelling development and strong monsoon wind periods. For the sake of readability and simplicity, we therefore use the three periods defined above for the diagnostics used to study OFU, SCU and MKU. Figure 3a,b,c,d shows for each period the maps of ensemble average of wind stress and wind stress curl, of surface current speed and of surface current vorticity averaged over the period, and the maps of relative intrinsic variability (IV_{tm}) of surface current vorticity over the period. A high (low) value of IV_{tm} of current vorticity indicates a strong (weak) OIV and a chaotic (stable) circulation. To quantify the strength of the eastward jet, we calculate the ensemble mean of the average surface current speed through the meridional transect at 109.9°E, between 9.5 and 12.2°N (red line in Figure 3a) during the three periods.

During the June period, the area of strong positive wind stress curl extends from the coast to ~113°E, with a narrow meridional coverage (Figure 3a). The ACC dipole is not clearly formed (Figure 3b,c). The weak eastward jet is located in the south with a maximum speed of 0.5-0.7 m.s^{-1} around 10-11°N, and a mean speed of 0.51 m.s^{-1}. The circulation is stable in the coastal jet area (IV_{tm} of current vorticity <50%, Figure 3d), but much more chaotic over most of the offshore area (IV_{tm} >200%). During the July period, the area of strong positive wind stress curl is larger than in June (from 10.5°N to 13°N, extending to 112°E). The eastward jet strengthens, with a mean speed of 0.78 m.s^{-1}, and is more in the north, with a speed of about 0.8-1.1m.s^{-1} near 11-12°N. The ACC dipole, with an anticyclonic (cyclonic) circulation in the south (north), is more pronounced than in June. The circulation is more stable than in June in the coastal zone and in the cyclonic and anticyclonic areas (IV_{tm} of current vorticity ~ 100%). It is less stable in the northeastern region of boxOF, where IV_{tm} exceeds 200%. During the August period, the area of strong positive wind stress curl has the largest meridional and zonal extent, to 114°E. The eastward jet is still stronger, with velocities reaching 1.2-1.5 m.s^{-1} around 10.5-11.5°N and a mean speed up to 0.88 m.s^{-1}. The ACC dipole is also stronger, with a well-established and large cyclonic gyre. The surface circulation is more stable compared to June and July, with a larger area of low IV_{tm} of current vorticity (<100%) covering boxOF. In September, the summer monsoon and the large-scale jet/ACC circulation begin to weaken (not shown).

4. Intraseasonal variability of upwelling

Here we examine the upwelling intraseasonal variability and its intrinsic variability for each upwelling area. Table 1 shows for the four areas the value of yearly upwelling index $UI_{JJAS,boxN}$ for each member and for the ensemble average, and its relative intrinsic variability $IV_{tm} (UI_{JJAS,boxN})$. It also shows the values of the correlation coefficients between the daily time series of the ensemble mean of $UI_{d,boxN}$ and of the wind stress components and intensity. Figure 3e,f shows for each period defined in Section 3 the maps of UI_d on the day of maximum $UI_{d,boxN}$ over each period and the maps of its relative intrinsic variability $IV_{tm} (UI_d)$.

4.1. The southern coastal upwelling (SCU)

For SCU, $UI_{d,boxSC}$ time series show a similar daily chronology for each member and for the ensemble mean (Figure 2b). SCU begins to develop during the first half of June, lasts during the whole summer with a strong intraseasonal variability, and disappears during the first half of September. We obtain three peaks of similar intensity, near June 19th, July 15th and August 16th, in phase with the wind forcing over the area: the correlation between the time series of $UI_{d,boxSC}$ and of the daily averaged wind stress intensity over boxSC is equal to 0.64 (p<0.01, Table 1). The correlation with the wind stress eastward component, i.e. the component nearly parallel to the south coast, that favors the SCU, reaches 0.71 (p<0.01).

Over the summer, $IV_d (UI_{d,boxSC})$ varies between 10% when SCU is weak and 40% during periods of strong SCU, showing similar values for the three upwelling peaks (Figure 2e). The yearly upwelling index $UI_{JJAS,boxSC}$ shows a weak ensemble standard deviation (7% relative to the mean, Table 1). This intrinsic variability of the SCU summer strength is much weaker than its interannual variability: in the 2009-2018 LONG simulation analyzed by To Duy et al. (2022), $UI_{JJAS,boxSC}$ shows a 53% interannual standard deviation relative to its interannual mean. SCU develops in the same area for the ten members, in the coastal zone of the ACC dipole convergence, as shown by

the very low values of IV_{tm} (UI_d) (<50%) over this area (Figure 3e,f). Higher IV_{tm} (UI_d) values are obtained at the periphery of this area, along the northern and southern flanks of the eastward jet. They are related to the variability of the meridional position of the jet: a jet located further north (south) induces a SCU further north (south).

SCU daily to intraseasonal variability is therefore mostly driven by the wind. The OIV is mainly related to the meridional position of the jet which does not vary much, thus affecting the SCU to second order at the intraseasonal scale.

4.2. The Mekong delta shelf upwelling (MKU)

For MKU, time series of $UI_{d,boxMK}$ are almost identical for each member and for the ensemble mean (Figure 2c). They also show a strong intraseasonal variability, with three peaks of varying intensity following the three wind peaks. The July peak is the strongest, followed by the August peak, then the June peak. The daily chronology of MKU also strongly follows the wind chronology, with a correlation of 0.65 (p<0.01) with the wind stress intensity averaged over MKU, and of 0.59 (0.61) with the wind stress eastward (northward) component (Table 1).

MKU is very weakly influenced by the OIV: $IV_d(UI_{JJAS,boxMK})$ never exceeds 30% (Figure 2e) and IV_{tm} $(UI_{JJAS,boxMK})$ is equal to 6% (Table 1). Again, this intrinsic variability of MKU summer strength is negligible compared to its interannual variability: the interannual standard deviation of $UI_{JJAS,boxMK}$ is equal to 85% in the LONG simulation (To Duy et al., 2022). Spatially, MKU is also very stable. As shown by To Duy et al. (2022), it develops along the northeastward current, behind Con Dao islands (Figures 1, 3e). For the 3 periods of MKU development, Figure 3d,f shows very weak values of IV_{tm} both for the surface current vorticity and for the spatial upwelling index. The circulation is therefore very stable in this area, explaining the spatial stability of MKU.

The daily chronology and intensity of MKU are thus mainly driven by the wind, and its position is determined by non-varying factors, presumably bathymetry, that still need to be investigated, and not by chaotic factors like (sub)mesoscale circulation. As a result, MKU is almost unaffected by OIV.

4.3. The offshore upwelling (OFU)

Again, the daily chronology of OFU is very similar for the ten members and the ensemble mean (Figure 2a), and in phase with the wind chronology (correlation of 0.65, p<0.01 with the daily wind stress intensity over boxOF, Table 1). However, contrary to SCU, the intensity of OFU peaks varies throughout the season, though wind stress intensity is similar during those peaks. We obtain two strong peaks (~1.0°C) in the heart of summer on July 19th and August 13th, a moderate peak (~0.6°C) at the end of August, and two small peaks (~0.2°C) at the beginning and end of summer, on June 18th and September 16th. $IV_d(UI_{d,boxOF})$ also varies a lot seasonally, and is maximum and much stronger than for SCU and MKU during OFU peaks (Figure 2e): it reaches 90% for the July peak, 70% during the August peaks, and respectively 30% and 50% during the small June and September peaks. On the summer average, IV_{tm} $(UI_{JJAS,boxOF})$ is equal to 18% (Table 1), again stronger than for SCU and MKU, but still much lower than the interannual variability (126%, To Duy et al., 2022). The regional daily wind stress therefore drives the daily to intraseasonal variability of OFU at the first order. However, OIV also significantly influences this daily variability, and this influence varies intraseasonally.

To understand the mechanisms that explain the intraseasonal variability of OFU intensity, we examine its functioning during its three main periods of OFU development (June, July and August, highlighted in blue in Figure 2). Da et al. (2019) and To Duy et al. (2022) showed that OFU is mainly induced by Ekman pumping and develops in the area of strong positive wind stress curl and current vorticity. The eastward jet and ACC dipole that favor the development of OFU are much stronger and well established in the heart of summer than at the beginning and end of the summer monsoon (Figure 3bc and Part 3). Northeastward wind intensity is stronger in July and August than in June and September (Figure 2) with a larger area of positive wind curl (Figure 3a). Moreover, positive current vorticity developing in boxOF in the area of positive wind curl is much stronger in July and August, which further enhances Ekman pumping (Figure 3e). The intraseasonal variability of OFU peaks is thus explained by the intraseasonal variability of wind and large-scale circulation.

We then examine the mechanisms that explain why the July and August peaks show different intrinsic variability but similar ensemble mean of OFU intensity (Figure 2a). Figure 4a shows the maps of UI_d on the day of maximum $UI_{d,boxOF}$ over the July OFU development period and the maps of average surface current vorticity during this period for 2 members of strong OFU (13, maximum $UI_{d,boxOF}$ = 1.53 °C; 17, maximum $UI_{d,boxOF}$ = 1.42 °C, Figure 2a) and 2 members of weak OFU (15, maximum $UI_{d,boxOF}$ = 0.77 °C; 18, maximum $UI_{d,boxOF}$ = 0.65 °C). In July, the eastward jet is much stronger than in June (Figure 3b,c and Section 3 above). OFU develops mainly in the area of positive wind stress curl and current vorticity along the northern flank of the jet (Figures 3c,e and 4). When the position of the eastward jet is located further south than average, as for members 13 and 17, the area of positive current vorticity northern of the jet in BoxOF coincides with the area of positive wind curl. This combination of positive current vorticity and positive wind curl enhances Ekman pumping induced upwelling (Figure 4) and results in a strong OFU covering a large area. This is the opposite when the position of the eastward jet is further north than average (members 15 and 18) : the area of positive current vorticity located in the positive wind curl region is smaller, not enhancing the Ekman pumping induced upwelling (Figure 4). Figure 3d,f shows strong values of IV_{tm} of current vorticity and upwelling intensity (> 100%) along the eastward jet and in the northeast area of boxOF. This confirms that OFU intrinsic variability in July is related to the effect of eastward jet meridional position variability on the circulation and on the upwelling that develops along the northern flank of the jet. Figure 4b shows the maps of UI_d on the day of maximum $UI_{d,boxOF}$ over the August OFU development period and the maps of average surface current vorticity and average wind stress curl during this period for 2 members of strong OFU (14, maximum $UI_{d,boxOF}$ = 1.65 °C; 13, maximum $UI_{d,boxOF}$ = 1.20 °C, Figure 2a) and 2 members of weak OFU (10, maximum $UI_{d,boxOF}$ = 0.82 °C; 16, maximum $UI_{d,boxOF}$ = 0.89 °C). In August, part of OFU still develops in the area of positive surface current vorticity along the northern flank of the eastward jet, but to less extent than in July (Figures 3e, 4). The meridional position of the jet does not vary a lot from one member to another (Figure 4b), as confirmed by the lower values of IV_{tm} of current vorticity in the jet area (Figure 3d). The eastward jet is thus stronger and more stable than in July (Figure 3b,c and Section 3), and does not induce a strong intrinsic variability of OFU. Instead, August OFU mainly develops in the area of positive vorticity north of the jet associated with the cyclonic eddy of the ACC dipole (Figures 4b,3e). Variations of zonal position of this eddy explain the variability of OFU intensity. From members 14, to 13, 10 and 16, this eddy is located more and more to the east, i.e. further and further away from the area of strong positive wind stress curl, resulting in a weaker and weaker OFU (Figures 4b). The variability of circulation in the northern part of boxOF therefore explains OFU intrinsic variability in August. This variability is moreover less than in July: IV_{tm} of current vorticity and of UI_d in

this northern part (highlighted by the black triangle in Figure 3d,e,f) is less in August than in July. The more stable jet in August, that results in a smaller intrinsic variability of OFU along the jet, and smaller intrinsic variability of current vorticity in the northern cyclonic part, where OFU mostly develops, therefore explain the intrinsic variability of OFU in August and the fact that it is smaller than in July.

In OFU, MKU and SCU areas, the effect of intrinsic variability on UI_d and the surface current vorticity therefore shows similar spatial patterns (Fig. 3d,f) and the influence of OIV on upwelling is directly linked to the influence of OIV on the circulation.

4.4. The northern coastal upwelling (NCU)

The ten members and the ensemble mean simulate NCU with a strong intraseasonal variability and a similar chronology (Figure 2d), completely different from the chronology obtained for the three other areas. A strong NCU develops at the beginning of summer (from June 10th to July 4th, reaching ~1.2°C for the ensemble average), and a weak NCU develops at the end of August (August 26th to 31st, reaching ~0.2°C). During those periods, highlighted in green in Figure 2, NCU chronology follows the wind chronology for the ten members: $UI_{d,boxNC}$ peaks correspond to peaks of northward (i.e. alongshore) wind favorable to NCU, around June 18th and 25th, July 2nd, and August 28th and 29th. There still a significant correlation between the time series of $UI_{d,boxNC}$ and the time series of wind stress northward component over boxNC, that favors the Ekman upwelling in this area (0.37, p<0.01, Table 1). It is however much weaker than correlations obtained for the other areas (at least 0.64). Moreover, although northward wind peaks occur during the whole summer (e.g July 17th - 22nd, highlighted in green in Figure 2) NCU does not develop from mid-July to mid-August.

NCU shows the strongest OIV of the four areas. $IV_d(UI_{d,boxNC})$ reaches 170% during the June-July peak, and is much smaller during the rest of the summer, reaching at most ~80% during the short late August peak (Figure 2e). The strong OIV in June explains the strong OIV at the summer scale (Table 1): $IV_{tm}(UI_{JJAS,boxNC})$ is equal to 37%, that is twice larger than for OFU and ~6 times larger than for SCU and MKU. It is about half the interannual variability of MKU summer strength (72% in the LONG simulation, To Duy et al., 2022).

These results suggest that the daily to intraseasonal chronology of upwelling in boxNC is partly driven by wind, but to less extent than in the other areas. Therefore other factors are involved that induce a strong intrinsic variability of NCU both at the daily and summer scales. To identify those factors, we use the three periods identified above : the period of strong wind over boxNC and strong NCU in June (June 10th – July 4th), the period of strong wind but no NCU in July (July 17th - 22nd), and the period of strong wind and weak NCU at the end of August (August 26th - 31st). We show in Figure 5 the maps of ensemble average of average surface current, current vorticity and IV_{tm} of current vorticity over each period, and the maps of UI_d and $IV_{tm}(UI_d)$ on the day of maximum $UI_{d,boxNC}$ over each period.

During the June period, ensemble average circulation in and around boxNC is globally offshore oriented. This favors the Ekman transport, hence the development of NCU. The ensemble spreading of NCU strength is very strong: $IV_{tm}(UI_d)$ spatially exceeds 300% in the eastern part of boxNC (Figure 5e), and $IV_d(UI_{d,boxNC})$ reaches 170% (Figure 2e). Figure 6 shows the maps of wind speed and curl, current speed and vorticity and UI_d on the day of maximum $UI_{d,boxNC}$ over the June period for two members of strong NCU (10 and 16) and two members of weak

341 NCU (09 and 11). A cyclonic gyre in the north and anticyclonic gyre in the south meet in boxNC for members 10

342 (between 13°N and 14°N) and 16 (between 14°N and 15°N). This induces a convergence and an offshore current

343 resulting in a strong upwelling, following the same mechanism as for SCU. For members 09 and 11, cyclonic and

344 anticyclonic gyres do not meet in boxNC, but either north or south of boxNC, not inducing offshore oriented

345 current over boxNC. Instead a weak NCU is induced by a favorable northward alongshore current in the northern

346 part of boxNC (Figure 6). As already observed at the interannual scale by To Duy et al. (2022) for the interannual

347 variability, mesoscale circulation of strongly chaotic nature in and around boxNC therefore drives the NCU

348 development and explains its high intrinsic variability during the June period. The effect of intrinsic variability on

349 NCU is not related to the intrinsic variability of current vorticity, but of current direction relative to the coast.

350 Between mid-July and mid-August, the large-scale circulation (ACC dipole and eastward jet) is strongly

351 established (see Section 3). The western part of the cyclonic eddy covers boxNC and induces a strong southward

352 alongshore current over this region. Close to the coast, this alongshore current is associated with a divergent

353 circulation, hence with a coastward component and a coastal downwelling which inhibits the NCU (see the high

354 negative vorticity in this area during the July period in Figure 5b). This large-scale ocean circulation is common

355 for the ten members and systematically prevents the NCU to develop (see the weak IV_{tm} of current vorticity and

356 the weak upwelling in Figure 5). This explains the very weak $UI_{d,boxNC}$ and $IV_d(UI_{d,boxNC})$ during this period (Figure

357 2e).

358 During the August period, the average circulation is similar to the mid-July and mid-August circulation described

359 above (Figure 5a,b). However, with the weakening of the summer monsoon, the ACC dipole structure

360 progressively weakens, the negative vorticity is less strong and the current is a bit more offshore oriented: NCU

361 is not as strong as in June, but it can develop easier than in the middle of the summer. $IV_d(UI_{d,boxNC})$ consequently

362 increases, but stays smaller than in June.

363 Our results therefore show that the development of NCU at the intraseasonal scale is first related to the large-scale

364 circulation, which prevents it during the heart of summer and allows it at the beginning and end of summer. Inside

365 those periods of "allowed NCU development", it is first driven by wind, then by the mesoscale circulation that

366 explains its very strong intrinsic variability.

367 **5. Conclusion and future work**

368 An ensemble of ten fine-resolution simulations with perturbed initial conditions was performed and analyzed in

369 this paper to represent and investigate (i) the daily to intraseasonal variability of ocean circulation and of SVU

370 over its different areas of development and (ii) the influence of OIV.

371 The ensemble was used to examine the seasonal variability and intrinsic variability of the circulation in the SVU

372 region during summer 2018. In June, the eastward jet is weak and mainly located in the south, the ACC dipole is

373 not formed and the circulation is only stable in the coastal area. In July, the jet is stronger and the ACC dipole is

374 clearly formed. The circulation in the area of positive vorticity north of the jet is more stable. In August the

375 southwest monsoon wind is at its strongest and has the largest area of influence, inducing an even stronger

376 eastward jet and a pronounced ACC dipole. In August, the circulation is stable over a larger area than in July.

377 We then examined the seasonal variability and intrinsic variability of the upwelling.

378   For SCU, MKU and OFU, the daily chronology and intraseasonal variability of the upwelling are quite similar
379   and mainly driven by the summer monsoon wind, with upwelling maxima in phase with strong southwest wind
380   periods. Their intrinsic variability is much weaker than their interannual variability.

381   The development of MKU and SCU is related to ocean circulation processes, respectively the northeastward
382   current and eastward jet, that are spatially quite stable. As a result, MKU and SCU show a very weak (less than
383   10%) intrinsic variability in space and time, both at daily scale and on average over summer. Peaks of OIV are
384   related to peaks of upwelling intensity. SCU develops as long as wind conditions are favorable over the area of
385   the ACC dipole convergence, that does not vary much spatially. MKU develops along the northeastward current
386   that flows offshore the Mekong delta and is spatially very stable.

387   OFU shows stronger intrinsic variability (18%), both at daily scale and for the whole summer period, and also in
388   space. The seasonal variability of OFU intensity and intrinsic variability are not only driven by the wind, but also
389   related to the period of the season. The large-scale circulation (ACC dipole and eastward jet) that enhances the
390   Ekman pumping – induced OFU is weak in June and September, whereas it is strongly established in the heart of
391   summer in July and August. This explains the stronger OFU intensity and OIV during the July-August period.
392   Moreover, for similar OFU intensity, the impact of OIV is weaker in August than in July. In July, OFU mainly
393   develops along the northern flank of the eastward jet. The meridional position of this jet is quite variable,
394   explaining the strong intrinsic variability of the July OFU: a southern (northern) position of the jet induces a larger
395   (smaller) common area between positive curl of wind stress and current, hence induces a stronger (weaker)
396   upwelling. In August, this position is much more stable. Moreover, OFU mainly develops in the area of cyclonic
397   activity north of the jet, related to mesoscale eddies of strong chaotic nature. OFU intensity depends on the zonal
398   position of this cyclonic activity with respect to the wind curl: a cyclonic eddy (not) located in the area of strong
399   positive wind stress curl results in stronger (weaker) OFU. The circulation in this area is moreover more stable
400   than in July, explaining the weaker intrinsic variability in August.

401   NCU daily chronology and the intraseasonal variability is completely different from that found in the three other
402   areas, and its intrinsic variability is much larger. At the intraseasonal scale, the development of NCU is driven by
403   the large-scale circulation. During the heart of summer, from mid-July to end of August, the eastward jet and ACC
404   dipole are strongly established, inducing a strong southward alongshore current over boxNC which annihilates
405   NCU, explaining its very low intensity and intrinsic variability. At the beginning and, to less extent, end of
406   summer, the large-scale ACC dipole structure and associated eastward current are weaker, allowing offshore
407   current to develop. Inside these periods, NCU chronology is driven by the wind but also by the development (or
408   not) of offshore oriented currents related to the spatial organization of coastal eddies. NCU shows a strong intrinsic
409   variability related to strong chaotic variability of mesoscale structures with the order of magnitude similar to
410   interannual variability (37%).

411   We investigated here the effect of OIV on the circulation and upwelling in the SVU region, confirming that this
412   chaotic part of ocean variability here is mainly related to the small-scale structures, as previously shown for other
413   areas. Following this study as well as those of Da et al. (2019) and To Duy et al. (2022), we can draw some
414   perspectives on the application of research regarding the predictability of SVU at the intraseasonal to interannual
415   scale. The development of MKU and SCU, which is little affected by OIV, could be largely predicted using wind

forecasts, provided of course that these forecasts are reliable. At first order, OFU can be partially predicted from wind forecasts, but with uncertainties in its daily to summer integrated magnitude that can vary by a factor of 1.5 to 2 (see Figure 2 and Table 1). Wind forecasts could identify favorable/unfavorable periods for NCU development. However, favorable periods would be associated with large uncertainty in terms of NCU intensity, given the strong impact of OIV on NCU during these periods. Further studies are underway to investigate the influence of other factors, including rivers and tides. Chen et al. (2012) indeed suggested that tides could influence the SVU development. Tidal amplitude is particularly strong over the shallow Mekong shelf region (Phan et al. 2019) and moreover subject to the influence of the Mekong river waters. Both factors may therefore affect SVU development and variability, in particular over the MKU and SVU areas. We moreover developed an ocean-atmosphere regional coupled model that will allow to study the impact of upwelling on atmosphere and climate, at local and regional scales, that was studied until now using satellite data and an atmosphere-only model (Xie et al. 2003; Zheng et al., 2016; Yu et al., 2020). The impact of upwelling on the marine ecosystem should also be studied, using for example the dynamical-biogeochemical coupled model developed by Ulses et al. (2016) and Herrmann et al. (2017). Finally, the long-term evolution of the upwelling should be studied, in particular since Herrmann et al. (2020,2022) showed that summer monsoon winds may weaken in response to climate change. Last, the upwelling that develops offshore from the Mekong Delta, MKU, was revealed by To Duy et al. (2022) and confirmed by the present study, and the northern coastal upwelling, NCU, was revealed by Da et al. (2019) and confirmed by Ngo and Hsin (2021). Extremely few in-situ observations are available over these two areas, and field campaigns are therefore necessary to better understand their functioning. This study explored the impact of OIV on the South Vietnam Upwelling, but is more generally of interest for the scientific community working on the functioning and variability of upwellings and on the effect and modeling of OIV.

Code and data availability

The SYMPHONIE model is available on the webpage of the SIROCCO group, https://sirocco.obs-mip.fr/. Sea surface temperature, currents and windstress simulated by the ensemble over summer 2018 are freely available on https://doi.org/10.5281/zenodo.7504087.

Authors Contribution

Marine Herrmann, To Duy Thai and Claude Estournel designed the experiments and To Duy Thai carried them out. Marine Herrmann prepared the manuscript with contributions from all co-authors.

Competing interests

The authors declare that they have no conflict of interest.

Acknowledgements

451   This work is a part of LOTUS international joint laboratory (lotus.usth.edu.vn). PhD studies of To Duy Thai were
452   funded through an IRD ARTS grant and a "Bourse d'Excellence" from the French Embassy in Vietnam.
453   Numerical simulations were performed using CALMIP HPC facilities (project P13120) and the cluster OCCIGEN
454   from the CINES group (project DARI A0080110098). It was also supported by Vietnam Academy of Science and
455   Technology, grant coded QTFR02.02/23-24.

456   The authors warmly thank both reviewers for their constructive comments.

457

458

459 **Tables**

460 Table 1 : For each upwelling area: value of the yearly upwelling index $UI_{JJAS,boxN}$ for each member of the ensemble,

461 of the ensemble mean $mi(UI_{JJAS,boxN})$ and of $IV_{tm}(UI_{JJAS,boxN})$, and correlation coefficients between the daily times

462 series of the ensemble mean of the daily upwelling index $UI_{d,boxN}$ and of the wind stress eastward and northward

463 components and intensity. Only correlations associated with p-values <0.01 are shown.

Members	09	10	11	12	13	14	15	16	17	18	$m_i(UI_{JJAS,boxN})$ (°C)	$IV_{tm}(UI_{JJAS,boxN})$ (%)	Correlation between $m_i(UI_{d,boxN})$ and wind stress eastward component	Correlation between $m_i(UI_{d,boxN})$ and wind stress northward component	Correlation between $m_i(UI_{d,boxN})$ and wind stress intensity
BoxOF	0.32	0.35	0.26	0.39	0.37	0.39	0.26	0.26	0.42	0.31	0.33	18 %	0.62	0.62	0.65
BoxSC	1.25	1.35	1.25	1.49	1.39	1.42	1.27	1.38	1.48	1.29	1.36	7 %	0.60	0.71	0.64
BoxNC	0.11	0.24	0.08	0.15	0.17	0.14	0.25	0.25	0.26	0.13	0.18	37 %	--	0.37	--
BoxMK	0.18	0.18	0.19	0.19	0.17	0.18	0.17	0.18	0.2	0.17	0.18	6 %	0.59	0.61	0.65

464
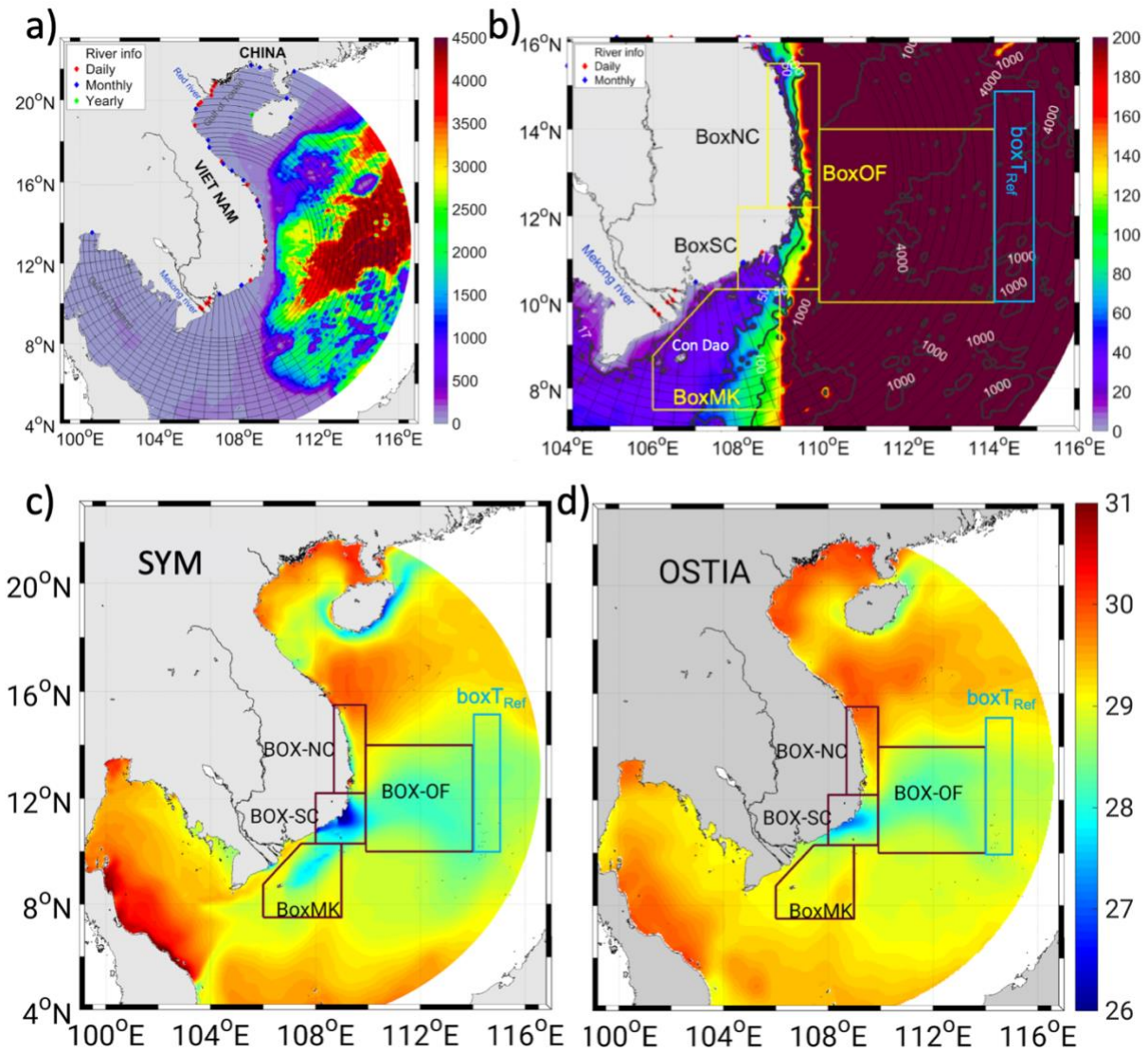
 Figures

Figure 1: (a) Characteristics of the orthogonal curvilinear computational grid (black lines, not all the mesh points are shown for visibility purposes) and bathymetry (colors, meter, *GEBCO_2014*) used for the VNC configuration of the SYMPHONIE model. Dots show the location of rivers for which we used daily (red), monthly (blue) and yearly climatology (green) discharge values (see To Duy et al. 2022 for more details). (b) Bathymetry (meter) over the SVU region. The 4 boxes used for the study of SVU are displayed in yellow. $boxT_{Ref}$ is highlighted in blue. (c,d) SST (°C) averaged over JJAS 2018 computed from the SYMPHONIE ensemble average (c) and from OSTIA reanalysis (d).

478
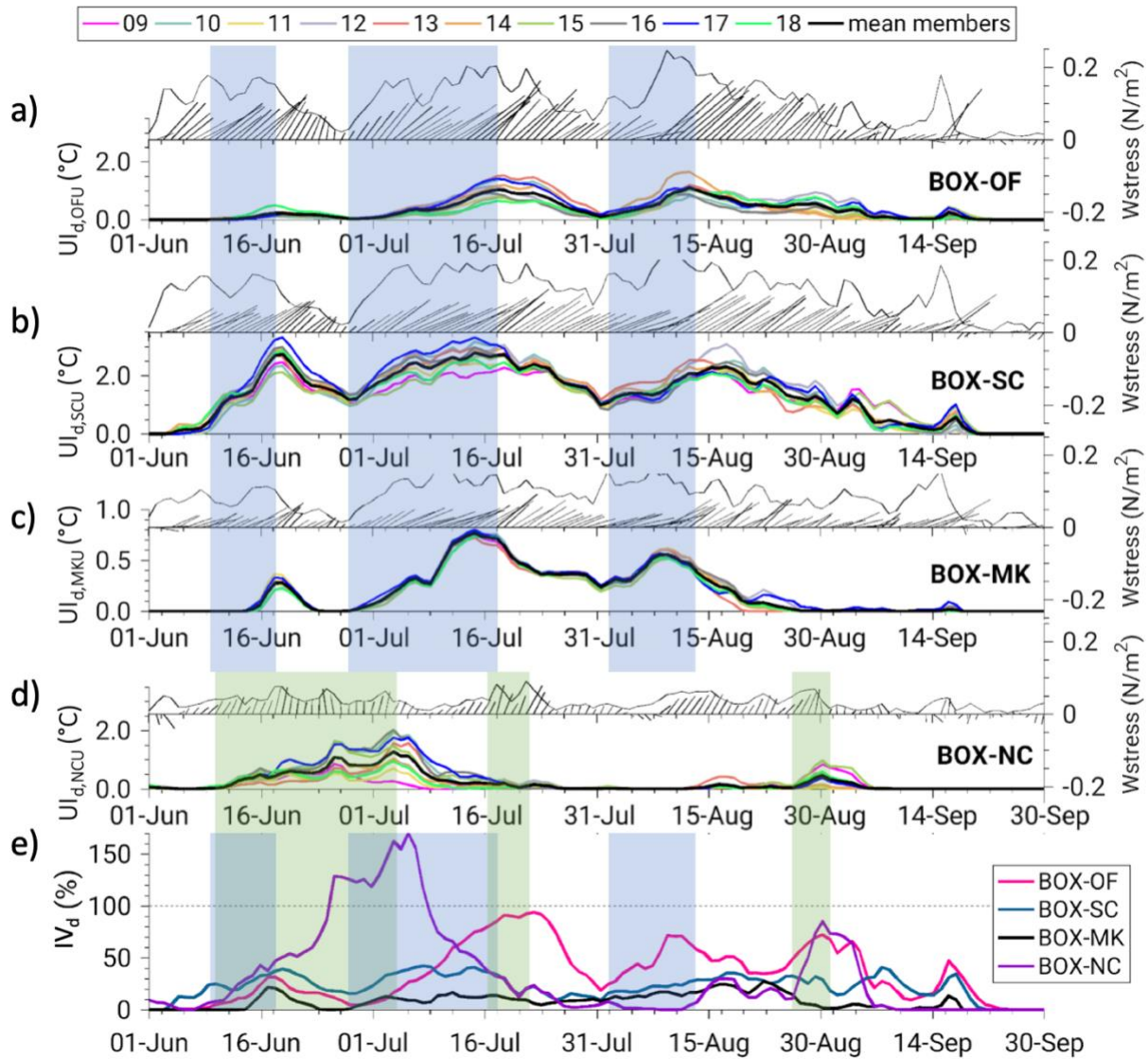
Figure 2: (a,b,c,d) Daily time series between June 1st and September 30th 2018 of direction (arrows) and intensity (black line) of spatially averaged wind stress (N.m^{-2}) over each upwelling area, and time series of $UI_{d,boxN}$ for each simulation (colored lines) and for the ensemble average (black thick line) for each upwelling area (a, BoxSC; b, BoxOF; c, BoxMK; d, BoxNC). (e) Daily time series of $IV_d(UI_{d,boxN})$ for each upwelling area. Periods covering OFU, SCU and MKU development are highlighted in blue. Periods used to study MKU development are highlighted in green.

485

486
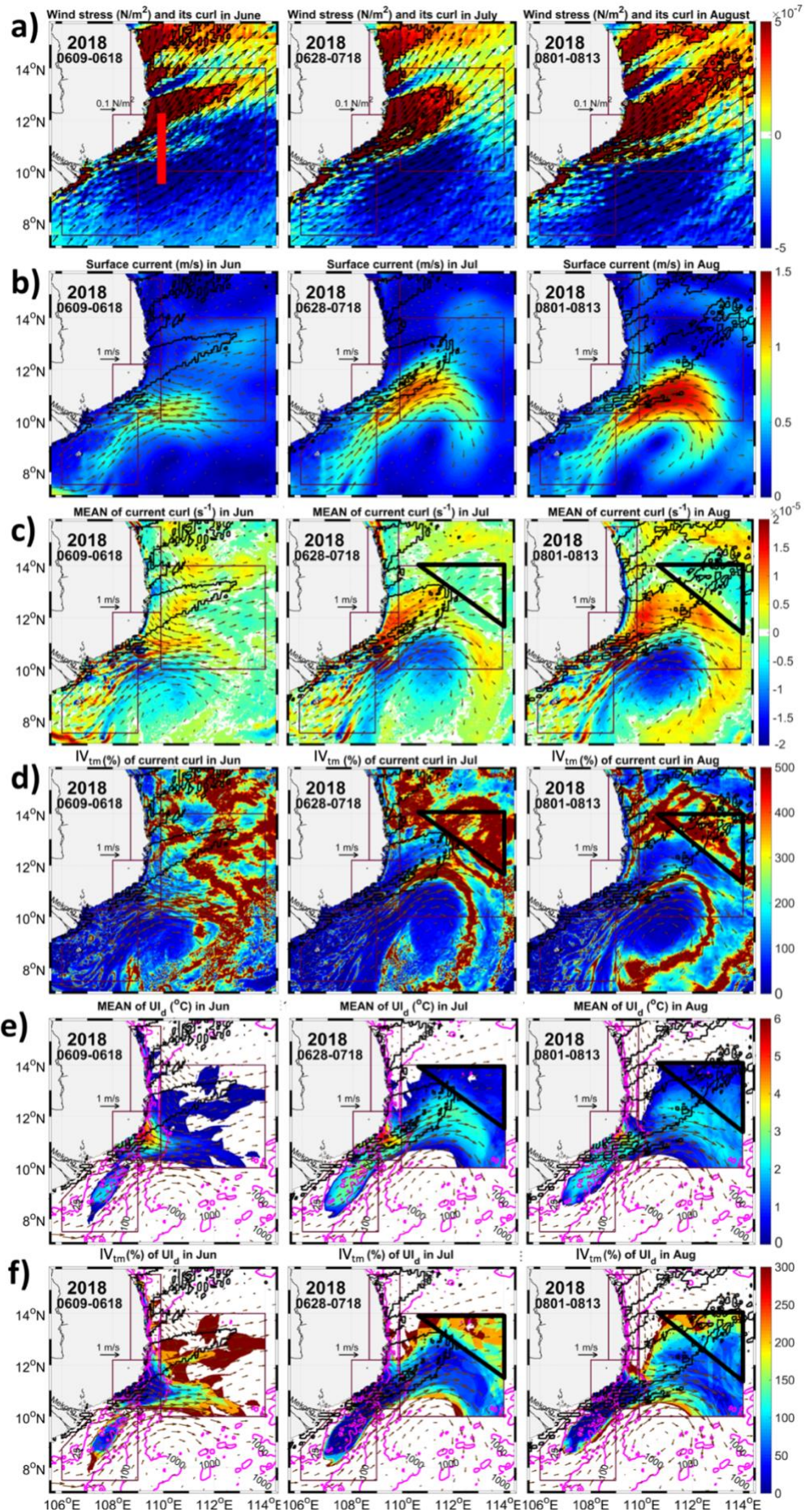
487   Figure 3: Maps of ensemble average of average wind stress (a, arrows, N.m^{-2}) and wind stress curl (a, colors, N.m^{-3}), of average surface current speed (b, m.s^{-1}) and vorticity (c, s^{-1}), of UI_d (e, °C) on the day of maximum $UI_{d,boxOF}$ over each period of OFU development highlighted in blue in Figure 2 (left June, middle July and right August), and maps of relative intrinsic variability (IV_{tm}) of average surface current vorticity (d, %) and of UI_d (f, %) over each period. Black lines: 3.10^{-7} N.m^{-3} iso-contours of average wind stress curl. Red segment (a): meridional transect at 109.9°E, 9.5 - 12.2°N used to compute the eastward jet strength. Arrows (b-f): average surface current during each period. Black triangles (c-f): area of large current vorticity north of the eastward jet during the July and August periods. Pink lines (e, f): isobaths (meters).

495
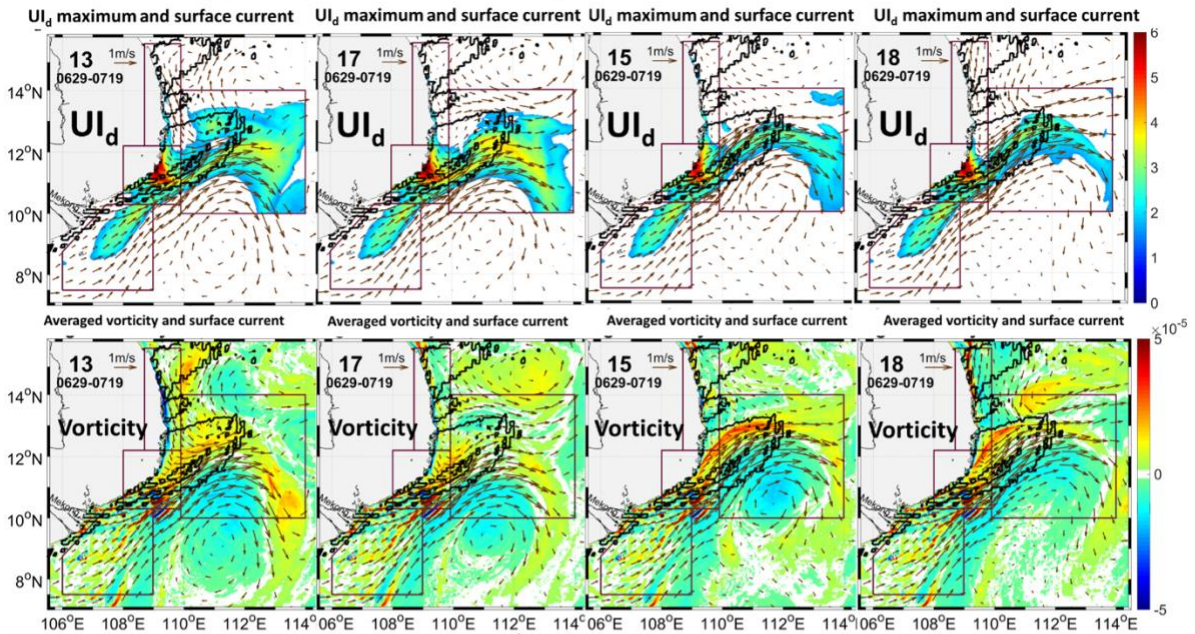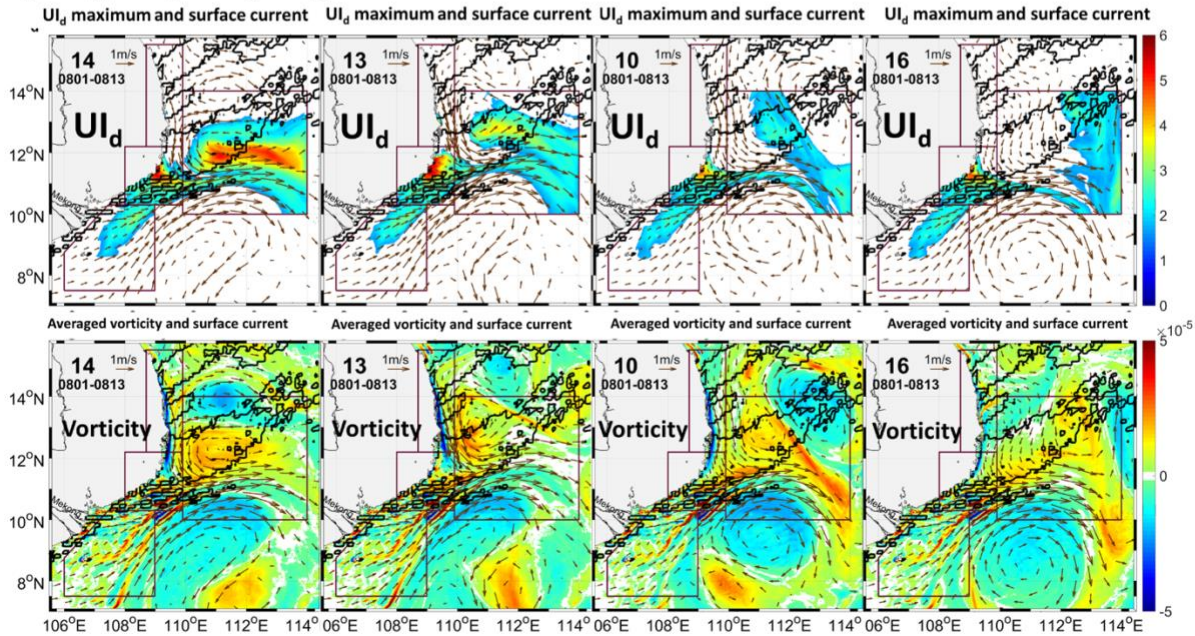
Figure 4: Maps of UI_d (top, °C) on the day of maximum $UI_{d,boxOF}$ over the periods of OFU development (highlighted in blue in Figure 2) in (a) July and (b) August, and of average surface current vorticity (bottom, s^{-1}) during each period for 2 members of strong OFU (members 13 and 17 for July, members 14 and 13 for August, Figure 2a) and 2 members of weak OFU (members 15 and 18 for July, members 10 and 16 for August). Black contours: 3.10^{-7} N.m^{-3} iso-contours of average wind stress curl during each period. Arrows: average surface current (m.s^{-1}).

505

506

507
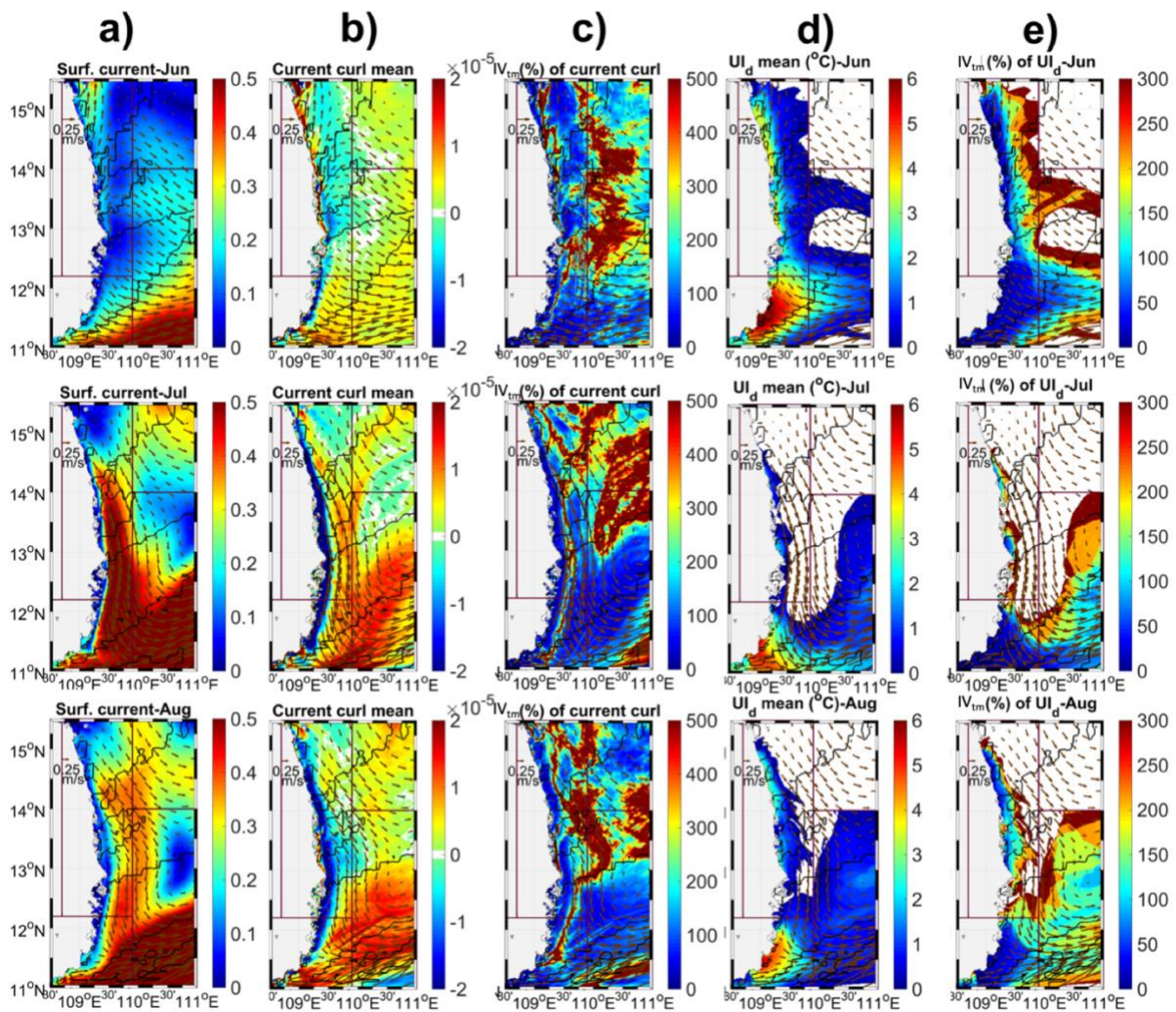
Figure 5 : Maps of ensemble average of average surface current speed (a, m.s^{-1}) and vorticity (b, s^{-1}) over each wind peak period over BoxNC (highlighted in green in Figure 2: 1st row June 10th – July 4th, 2nd row July 17th - 22nd and 3rd row August 26th - 31st), of UI_d (d, °C) on the day of maximum $UI_{d,boxNC}$ over each period, and of relative intrinsic variability IV_{tm} of average surface current vorticity (c, %) and UI_d (e, %) over each period. Black contours: 3.10^{-7} N.m^{-3} iso-contours of average wind stress curl during each period. Arrows: average surface current (m.s^{-1}).

514
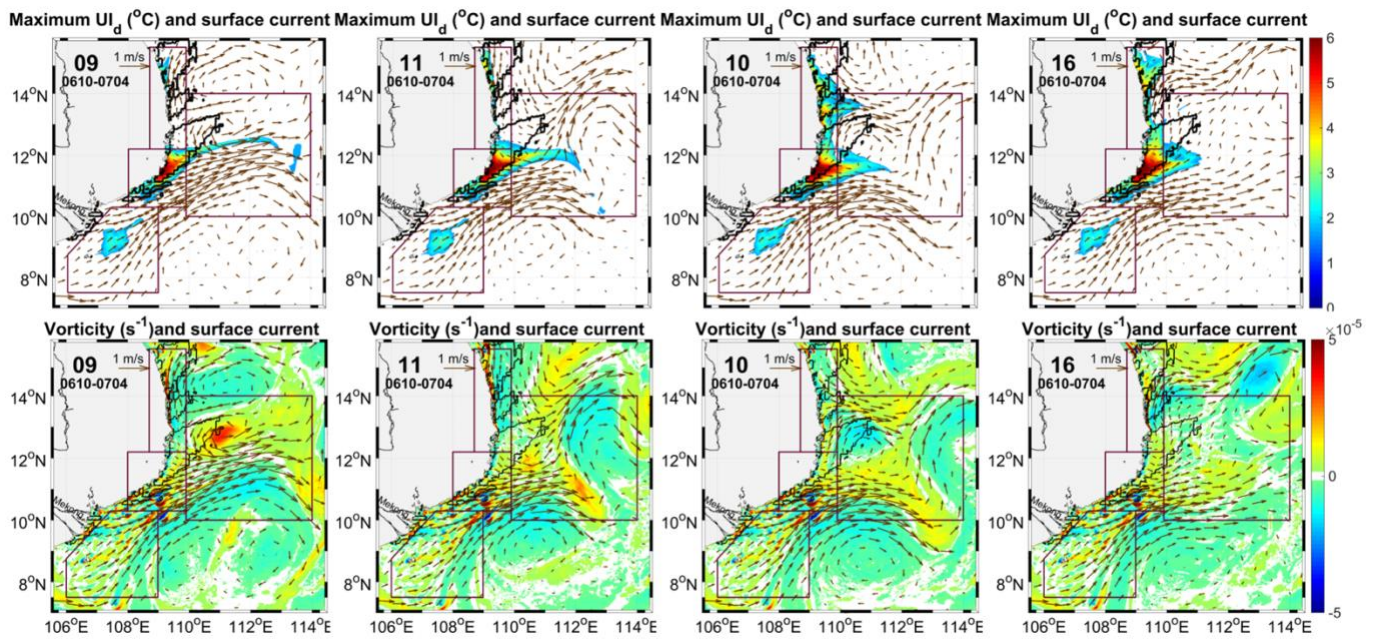
515

516

517 Figure 6 : Maps of UI_d (1st row, °C) on the day of maximum $UI_{d,boxNC}$ over the July wind peak period over BoxNC

518 (highlighted in green in Figure 2) and maps of average surface current vorticity (2nd row, s^{-1}) for 2 members of

519 weak NCU (9, 11) and 2 members of strong NCU (10, 16) during the June-July period. Black contours: 3.10^{-7}

520 N.m^{-3} iso-contours of average wind stress curl during each period. Arrows: average surface current (m.s^{-1}).

521

522   References

523   Bombar, D., Dippner, J. W., Doan, H. N., Ngoc, L. N., Liskow, I., Loick-Wilde, N., and Voss, M.: Sources of
524   new nitrogen in the Vietnamese upwelling region of the South China Sea, J. Geophys. Res. Ocean., 115, 6018,
525   https://doi.org/10.1029/2008JC005154, 2010.

526   Chen, C. and Wang, G.: Interannual variability of the eastward current in the western South China Sea associated
527   with   the   summer   Asian   monsoon,   J.   Geophys.   Res.   Ocean.,   119,   5745–5754,
528   https://doi.org/10.1002/2014JC010309, 2014.

529   Chen, C., Lai, Z., Beardsley, R. C., Xu, Q., Lin, H., and Viet, N. T.: Current separation and upwelling over the
530   southeast   shelf   of   Vietnam   in   the   South   China   Sea,   J.   Geophys.   Res.   Ocean.,   117,   1–16,
531   https://doi.org/10.1029/2011JC007150, 2012.

532   Da, N. D., Herrmann, M., Morrow, R., Niño, F., Huan, N. M., and Trinh, N. Q.: Contributions of Wind, Ocean
533   Intrinsic Variability, and ENSO to the Interannual Variability of the South Vietnam Upwelling: A Modeling
534   Study, J. Geophys. Res. Ocean., 124, 6545–6574, https://doi.org/10.1029/2018JC014647, 2019.

535   Dippner, J. W., Nguyen, K. V., Hein, H., Ohde, T., and Loick, N.: Monsoon-induced upwelling off the Vietnamese
536   coast, Ocean Dyn., 57, 46–62, https://doi.org/10.1007/S10236-006-0091-0, 2007.

537   Herrmann, M., Auger, P. A., Ulses, C., and Estournel, C.: Long-term monitoring of ocean deep convection using
538   multisensors   altimetry   and   ocean   color   satellite   data,   J.   Geophys.   Res.   Ocean.,   122,   1457–1475,
539   https://doi.org/10.1002/2016JC011833, 2017.

540   Herrmann, M., Ngo-Duc, T., and Trinh-Tuan, L.: Impact of climate change on sea surface wind in Southeast Asia,
541   from climatological average to extreme events: results from a dynamical downscaling, Clim. Dyn. 2020 543,
542   54, 2101–2134, https://doi.org/10.1007/S00382-019-05103-6, 2020.

543   Herrmann, M., Nguyen-Duy, T., Ngo-Duc, T., and Tangang, F.: Climate change impact on sea surface winds in
544   Southeast Asia, Int. J. Climatol., 42, 3571–3595, https://doi.org/10.1002/JOC.7433, 2022.

545   Isoguchi, O., and Kawamura, H.: MJO-related summer cooling and phytoplankton blooms in the South China Sea
546   in recent years, Geophys. Res. Lett., 33, L16615, doi:10.1029/2006GL027046, 2006.

547   Kuo, N. J., Zheng, Q., and Ho, C. R.: Response of Vietnam coastal upwelling to the 1997-1998 ENSO event
548   observed by multisensor data, Remote Sens. Environ., 89, 106–115, https://doi.org/10.1016/j.rse.2003.10.009,
549   2004.

550   Li, Y., Han, W., Wilkin, J. L., Zhang, W. G., Arango, H., Zavala-Garay, J., Levin, J., and Castruccio, F. S.:
551   Interannual variability of the surface summertime eastward jet in the South China Sea, J. Geophys. Res.
552   Ocean., 119, 7205–7228, https://doi.org/10.1002/2014JC010206, 2014.

553   Liu, X., Wang, J., Cheng, X., and Du, Y.: Abnormal upwelling and chlorophyll-a concentration off South Vietnam
554   in summer 2007, J. Geophys. Res. Ocean., 117, 2–11, https://doi.org/10.1029/2012JC008052, 2012.

555   Loick-Wilde, N., Bombar, D., Doan, H. N., Nguyen, L. N., Nguyen-Thi, A. M., Voss, M., and Dippner, J. W.:
556   Microplankton biomass and diversity in the Vietnamese upwelling area during SW monsoon under normal
557   conditions   and   after   an   ENSO   event,   Prog.   Oceanogr.,   153,   1–15,
558   https://doi.org/10.1016/j.pocean.2017.04.007, 2017.

559   Lu, W., Oey, L. Y., Liao, E., Zhuang, W., Yan, X. H., and Jiang, Y.: Physical modulation to the biological
560   productivity   in   the   summer   Vietnam   upwelling   system,   Ocean   Sci.,   14,   1303–1320,
561   https://doi.org/10.5194/OS-14-1303-2018, 2018.

Lyard, F., Lefevre, F., Letellier, T., and Francis, O.: Modelling the global ocean tides: modern insights from FES2004, Ocean Dyn. 2006 565, 56, 394–415, https://doi.org/10.1007/S10236-006-0086-X, 2006.

Marsaleix, P., Auclair, F., Floor, J. W., Herrmann, M. J., Estournel, C., Pairaud, I., and Ulses, C.: Energy conservation issues in sigma-coordinate free-surface ocean models, Ocean Model., 20, 61–89, https://doi.org/10.1016/j.ocemod.2007.07.005, 2008.

Marsaleix, P., Michaud, H., and Estournel, C.: 3D phase-resolved wave modelling with a non-hydrostatic ocean circulation model, Ocean Model., 136, 28–50, https://doi.org/10.1016/J.OCEMOD.2019.02.002, 2019.

Ngo, M. H. and Hsin, Y. C.: Impacts of Wind and Current on the Interannual Variation of the Summertime Upwelling Off Southern Vietnam in the South China Sea, J. Geophys. Res. Ocean., 126, e2020JC016892, https://doi.org/10.1029/2020JC016892, 2021.

Pairaud, I., Lyard, F., Auclair, F., Letellier, T., and Marsaleix, P.: Dynamics of the semi-diurnal and quarter-diurnal internal tides in the Bay of Biscay. Part 1: Barotropic tides, Cont. Shelf Res., 28, 1294–1315, https://doi.org/10.1016/J.CSR.2008.03.004, 2008.

Pairaud, I., Staquet, C., Sommeria, J., and Mahdizadeh, M. M.: Generation of harmonics and sub-harmonics from an internal tide in a uniformly stratified fluid: Numerical and laboratory experiments, 28, 51–62, https://doi.org/10.1007/978-94-007-0360-5_5/COVER/, 2010.

Penduff, T., Juza, M., Barnier, B., Zika, J., Dewar, W. K., Treguier, A. M., Molines, J. M., and Audiffren, N.: Sea level expression of intrinsic and forced ocean variabilities at interannual time scales, Journal of Climate, 24, 5652–5670. https://doi.org/10.1175/JCLI-D-11-00077.1, 2011

Phan, H. M., Ye, Q., Reniers, A. J.H.M., Stive, M. J. F: Tidal wave propagation along The Mekong deltaic coast, Estuarine, Coastal and Shelf Science, 220, 73-98, https://doi.org/10.1016/j.ecss.2019.01.026; 2019

Sérazin, G., Meyssignac, B., Penduff, T., Terray, L., Barnier, B., and Molines, J. M.: Quantifying uncertainties on regional sea level change induced by multidecadal intrinsic oceanic variability, Geophys. Res. Lett., 43, 8151–8159, https://doi.org/10.1002/2016GL069273, 2016.

To Duy, T., Herrmann, M., Estournel, C., Marsaleix, P., Duhaut, T., Bui Hong, L., and Trinh Bich, N.: Role of wind, mesoscale dynamics and coastal circulation in the interannual variability of South Vietnam Upwelling, South China Sea. Answers from a high resolution ocean model, Ocean Sci., 18, 1131–1161, https://doi.org/10.5194/os-18-1131-2022, 2022

Ulses, C., Auger, P. A., Soetaert, K., Marsaleix, P., Diaz, F., Coppola, L., Herrmann, M. J., Kessouri, F., and Estournel, C.: Budget of organic carbon in the North-Western Mediterranean open sea over the period 2004–2008 using 3-D coupled physical-biogeochemical modeling, J. Geophys. Res. Ocean., 121, 7026–7055, https://doi.org/10.1002/2016JC011818, 2016.

Waldman, R., Herrmann, M., Somot, S., Arsouze, T., Benshila, R., Bosse, A., Chanut, J., Giordani, H., Sevault, F. and Testor, P.: Impact of the Mesoscale Dynamics on Ocean Deep Convection: The 2012-2013 Case Study in the Northwestern Mediterranean Sea, J. Geophys. Res. Oceans., 122, 8813– 8840, doi:10.1002/2016JC01258, 2017b.

Waldman, R., Somot, S., Herrmann, M., Sevault, F., and Isachsen, P. E.: On the Chaotic Variability of Deep Convection in the Mediterranean Sea, Geophys. Res. Lett., 45, 2433–2443, https://doi.org/10.1002/2017GL076319, 2018.

Waldman, R., Somot, S., Herrmann, M., Bosse, A., Caniaux, G., Estournel, C., Houpert, L., Prieur, L., Sevault, F., and Testor, P.: Modeling the intense 2012–2013 dense water formation event in the northwestern

603 Mediterranean Sea: Evaluation with an ensemble simulation approach, J. Geophys. Res.
604   Oceans, 122, 1297– 1324, doi:10.1002/2016JC012437, 2017a.

605 Wang, B., LinHo, Zhang, Y., and Lu, M. M.: Definition of South China Sea monsoon onset and commencement
606   of the East Asian summer monsoon, J. Clim., 17, 699–710, https://doi.org/10.1175/2932.1, 2004.

607 Wang, Y., Fang, G., Wei, Z., Qiao, F., and Chen, H.: Interannual variation of the South China Sea circulation and
608   its relation to El Niño, as seen from a variable grid global ocean model, J. Geophys. Res. Ocean., 111, 1–15,
609   https://doi.org/10.1029/2005JC003269, 2006.

610 Wyrtki, K.: Physical oceanography of the South East Asian Waters, Naga Rep., 2, 1961.

611 Xie, S.-P., Xie, Q., and Wang, D.: Summer Upwelling in the South China Sea and its Role in Regional Climate
612   Variations, J. Geophys. Res., 108, 1–37, https://doi.org/10.1029/2003JC001867, 2003.

613 Xie, S. P., Chang, C. H., Xi, Q., and Wang, D.: Intraseasonal variability in the summer South China Sea: Wind
614   jet, cold filament, and recirculations, J. Geophys. Res. Ocean., 112, 1–11,
615   https://doi.org/10.1029/2007JC004238, 2007.

616 Yu, Y., Wang, Y., Cao, L., Tang, R. and Chai, F.: The ocean-atmosphere interaction over a summer upwelling
617   system in the South China Sea, Journal of Marine Systems, 208, 103360,
618   https://doi.org/10.1016/j.jmarsys.2020.103360, 2020.

619 Zheng, Z. W., Zheng, Q., Kuo, Y. C., Gopalakrishnan, G., Lee, C. Y., Ho, C. R., Kuo, N. J., and Huang, S. J.:
620   Impacts of coastal upwelling off east Vietnam on the regional winds system: An air-sea-land interaction, Dyn.
621   Atmos. Ocean., 76, 105–115, https://doi.org/10.1016/j.dynatmoce.2016.10.002, 2016.